ADVANCED MATERIALS

Supporting Information

High-Resolution and High-Throughput Plasmonic Photopatterning of Complex Molecular Orientations in Liquid Crystals

Yubing Guo, Miao Jiang, Chenhui Peng, Kai Sun, Oleg Yaroshchuk, Oleg Lavrentovich, and Qi-Huo Wei*

Supporting Information

High Resolution and High Throughput Plasmonic Photopatterning of Complex Molecular Orientations in Liquid Crystals

Yubing Guo, Miao Jiang, Chenhui Peng, Kai Sun, Oleg Yaroshchuk, Oleg Lavrentovich, Qi-Huo Wei*

[*] Yubing Guo, Miao Jiang, Chenhui Peng, Prof. Oleg Lavrentovich, Prof. Qi-Huo Wei
Liquid Crystal Institute, Kent State University, Kent, OH44242, USA
E-mail: qwei@kent.edu

Dr. Kai Sun
Department of Material Science and Engineering, University of Michigan, Ann Harbor, MI48109, USA

Prof. Oleg Yaroshchuk
Institute of Physics, National Academy of Sciences of Ukraine, Kyiv 03028, Ukraine

1. Absorption Spectra of Brilliant Yellow and PAAD-72

The brilliant yellow and PAAD-72 are bought from Sigma-Aldrich and Beam Co respectively,

and used without further purification. To measure the absorption spectra of brilliant yellow
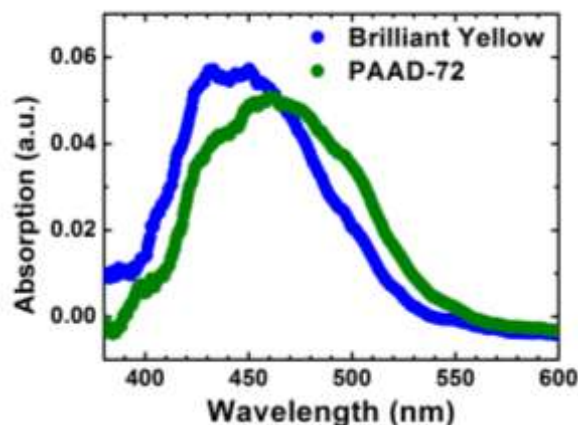

Figure S1. Absorption Spectrum. Measured absorption spectra for thin films of
brilliant yellow and PAAD-72.

and PAAD-72, we spin-coated thin films of them on glass substrates with 1500 rpm. The

PAAD-72 is used as received without dilution. As for brilliant yellow, we tried different

concentrations and found that 0.5wt% in dimethylformamide (DMF) yields a good

photoalignment with slightly longer exposure time than PAAD-72. The absorption spectra of

these thin films were measured after 20 min baking on a 90°C hot stage. Both the brilliant

yellow and PAAD-72 provide excellent planar alignments of LC molecules, which is in

agreement with previous studies[1,2].

2. Simulation Studies of Plasmonic Metamasks (PMMs)

We have performed numerical simulations to optimize the PMM transmission and polarization contrast. To simplify the notation, the short axis of the nanoapertures is oriented along the *x*-axis and the long axis of nanoapertures is oriented along the *y*-axis. Accordingly the transmittance for polarization along the *x*-axis is referred to as the TM transmittance.

Firstly, we compared square and triangular lattice of parallel rectangular nanoapertures. The results show that for the same size and periodicity of the nanoapertures and the same film
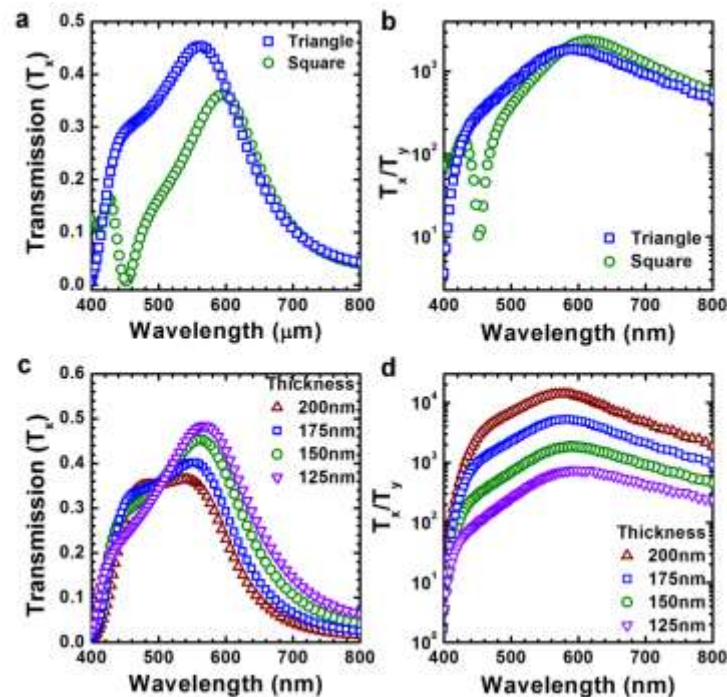
Figure S2. Effects of the lattice and mask thickness. a, b) Exemplary TM transmission spectra (a) and polarization contrast spectra (b) for the triangular and square lattices of rectangular nanoapertures in a 150 nm thick metamask. c, d) TM transmission spectra (c) and polarization contrast spectra (d) for the triangular lattices of rectangular nanoapertures with different Al film thicknesses. In a-d) the nanoaperture size is fixed at 100 nm × 220 nm, and the lattice constants are at 300 nm for both triangular and square lattices.

thickness, the triangular lattice yields roughly 50% higher optical transmission and better polarization contrast in the wavelength range between 400nm and 600nm (Figure S2a-b). This can be attributed in one part to the fact that the nanoaperture density in the triangular lattice is

15% higher than that in the square lattice and in the other part to different plasmon coupling

between neighboring apertures.

Then we studied the effects of the mask thickness on the optical transmission and
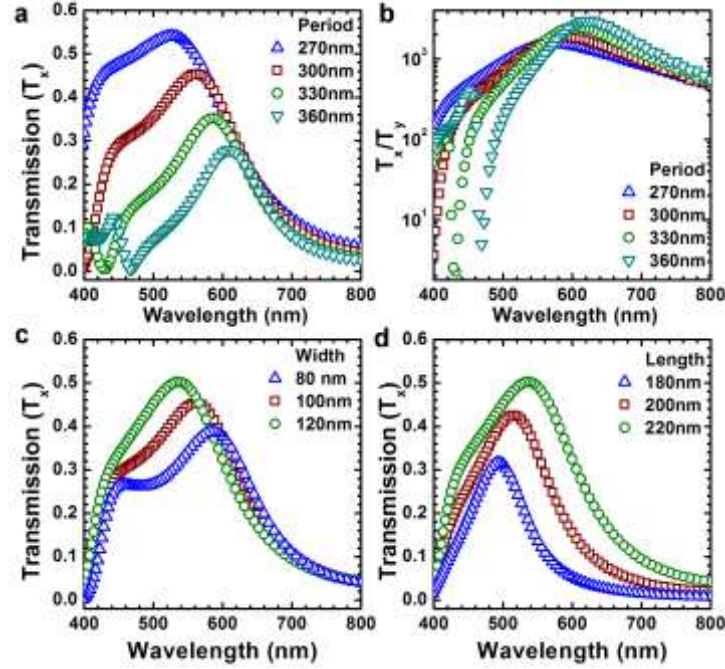

Figure S3. Effects of the periodicity and nanoaperture size/shape: a) Simulated TM transmission spectra for triangular lattices of parallel rectangular nanoapertures with four different periodicities. The polarization of the incident light is perpendicular to the nanoaperture. b) Simulated polarization ratio for the same nanoaperture parameters in a). The nanoaperture size in a) and b) is 100 nm × 220 nm. c, Simulated TM transmission spectra for nanoaperture length = 220 nm and width = 80 nm, 100 nm, and 120 nm. d) Simulated TM transmission spectra for nanoaperture width = 120 nm and length = 180 nm, 200 nm, and 220 nm. The nanoaperture period is 300 nm in c) and d).

polarization contrast for the triangular lattices of parallel nanoapertures. We can see that there

are two transmission peaks which exhibit different dependence on the film thickness (Figure

S2c). With the increase of the mask thickness, the left peak remains in the same position

while the right peak shifts to the left. This behavior suggests that the two peaks are caused by

two different physical mechanisms. In contrast, the polarization contrast increases

monotonically with the mask thickness at all wavelengths (Figure S2d).

As a trade-off between the transmittance and polarization contrast, we fixed the mask thickness at 150 nm and explored the effects of the lattice period. For the nanoapertures of 100 nm × 220 nm in size, we can see that with the decrease of lattice period, the transmittance for polarization perpendicular to the nanoaperture long axis (or TM transmission) goes up monotonically while the locations of both peaks shift to the shorter wavelengths and the polarization contrast exhibits minor increases (Figure S3a-b).

We also investigated the effect of nanoaperture size on the optical transmission (Figure S3c-d). We found that the left peak is insensitive to the aperture size variation while the right peak exhibits strong dependences on the nanoaperture size. In particular, the right peak shifts to a shorter wavelength when the nanoaperture width is increased and to a longer wavelength when the nanoaperture length is increased.
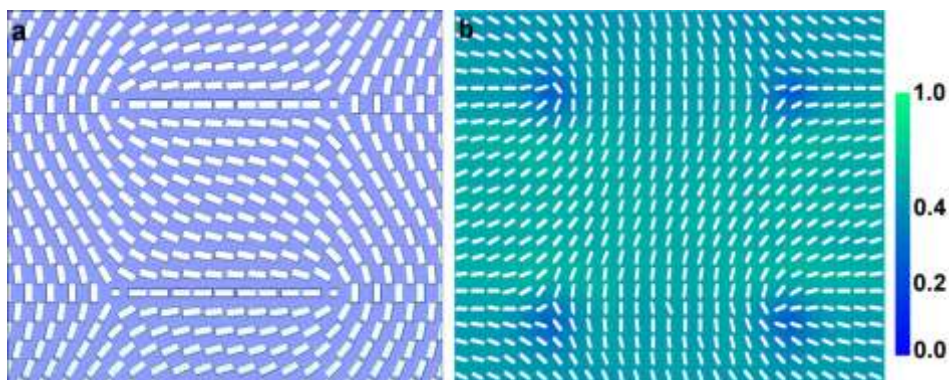

Figure S4. Exemplary Polarization Patterns: a) Schematic metamask where the nanoapertures form two -1/2 and two +1/2 defects. Here the period of the triangular lattice is 270 nm, the size of the nanoapertures is 100nm × 220nm, and the boundary condition is periodic. B) Calculated local polarization directions (white rods) at a plane located 500nm above the Al mask. The background color represents local optical transmittance.

To illustrate the capability of PMMs in generating complex polarization patterns, we simulated arrays of nanoapertures which are oriented to form 1/2 and -1/2 defects (Figure S4). This is similar to the PMM shown in Figure 3a. We illuminated the mask with circular polarized light and calculated the polarization directions in a plane located at 500 nm above the Al film. It can be seen that the local polarization of the transmitted light is perpendicular

to the local nanoaperture orientations; the transmitted optical field thus forms optical vortices centered at the disclinations cores. The electrical field strength at the centers of these vortices defect centers is minimal. This is expected because the vortices are singular lines where the polarization directions are undefined and the intensities should be zero.

3 Physical Mechanisms for the Enhanced Optical Transmissions

Given the subwavelength sizes of these nanoapertures, the optical transmissions approaching 50% are extraordinary. Since the first observation of the extraordinary optical transmission[3,4], extensive theoretical and experimental studies revealed that the resonant excitations of surface waves and cavity modes are two major physical mechanisms[5-9]. There are studies dedicated to the extraordinary optical transmission through rectangular hole arrays[10-14], which involves lattices, materials and aperture sizes different from those used in our metamasks. Here we discuss the physical mechanisms behind these two peaks in the simulated optical transmission spectra.

The properties of the left peak in transmission spectra, namely its dependence on arrays periodicity and its insensitivity to the nanoaperture size (width, length and depth) suggest that the extraordinary high optical transmission originates from the excitation of surface waves. Theoretical studies show that both cylindrical waves and surface plasmon waves contribute to the transmission. Particularly, we found that the wavelength of the left transmission peak is corresponding to the excitation of surface plasmon waves in the metal-SiO_2 interface or $\lambda = a\sqrt{\varepsilon_m \varepsilon_d / (\varepsilon_m + \varepsilon_d)}$, where a is the triangular lattice period, ε_m is the permittivity of Al, and ε_d is the permittivity of SiO_2.

The dependence of the right peak on nanoaperture size (width, length and the mask thickness) indicates that cavity resonances are responsible for the transmission enhancements. Meantime, the variation of the peak wavelength with the periodicity suggests that these cavity modes are coupled. The nanoaperture can be considered as a rectangular waveguide in Al

where the confinement of two long Al walls leads to a propagating gap plasmon wave which is a TM wave[15-17]. Given that the two short sides of Al walls are parallel to the electrical field of the gap plasmon wave, their confinement induces a TE waveguide mode, or sets a wave vector k_x along the long axis of the aperture. For the lowest cavity mode the electrical field perpendicular to the long axis can be expressed as[15-17]:

$$E_y \sim \left[e^{-\gamma(y+w)} + e^{+\gamma(y-w)} \right] cos(k_x x) e^{ik_z z} \tag{S1}$$

where the first term is due to the surface plasmon waves at two long walls, the second term originates from the first TE mode, the third term indicates the propagation in the channel direction, and the nanoaperture width is assumed to be $2w$. Denoting the wave vector of light in air as k_0 and the vector of the gap surface plasmon wave as k_{gsp}, we have $k_0^2 = k_{gsp}^2 + (i\gamma)^2$. $k_{gsp}^2 = k_x^2 + k_z^2$. The dispersion relation for the anti-symmetric gap surface plasmon can be expressed as[15,18]:

$$tanh\left(-iw\sqrt{\varepsilon_d k_0^2 - k_{gsp}^2} \right) = -\frac{\varepsilon_D \sqrt{\varepsilon_m k_0^2 - k_{gsp}^2}}{\varepsilon_m \sqrt{\varepsilon_d k_0^2 - k_{gsp}^2}} \tag{S2}$$

where ε_m is the permittivity of Al, ε_d is the permittivity of the dielectric material in the gap which is 1 for air. The waveguide condition for the TE mode can be expressed as[15]:

$$tan\left(k_x l - \frac{(m-1)\pi}{2} \right) = \frac{\sqrt{k_z^2 - \varepsilon_m k_0^2}}{k_x} \tag{S3}$$

where $2l$ is the nanoaperture length, and $m = 1$ for the lowest TE mode.

Analytical expressions for the resonant condition of these modes inside the nanoapertures are difficult to derive since these nanocavities are coupled. A quantitative description of the cavity resonant conditions requires the microscopic theory which takes into account both the cavity modes and their coupling[6,19], which we leave for future studies.

.

4 PMMs and Photopatterning

Additional PMMs and their uses for photopatterning of different defect clusters and defect arrays are included here. Figure S5a-e presents the PMM and the photopatterned pair of +1/2 and -1/2 charge defects. Figure S6a-e presents the PMM and the photopatterned butterfly of one +1 and two -1/2 defects. Figure S7a-e presents the PMM and the photopatterned flower of one +2 and four -1/2 defects. Figure S8 presents the PMMs and the photopatterned defects arrays with (+3/2, -3/2) charges and (+2, -2) charges.
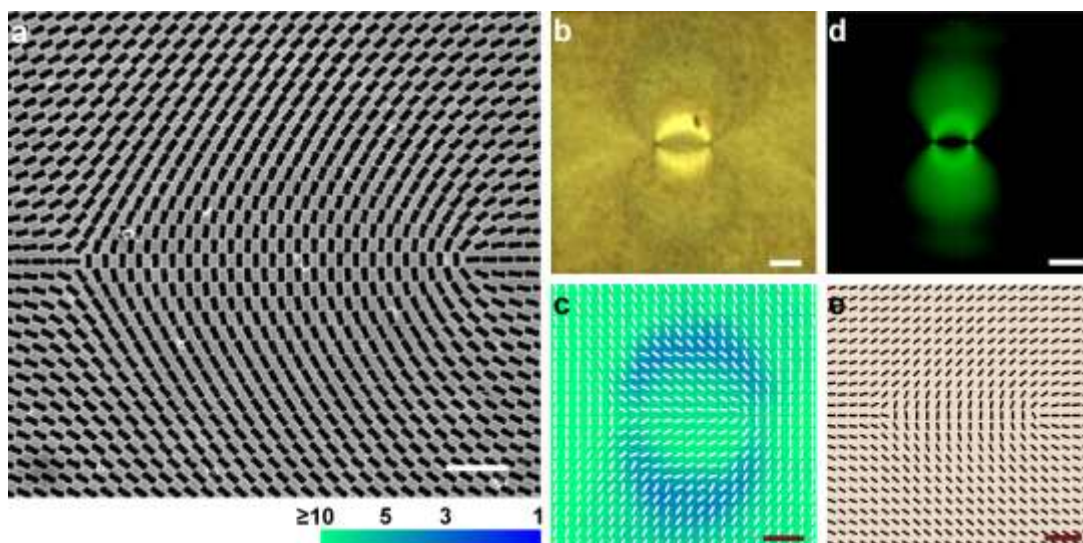

Figure S5 │ Plasmonic photopatterning of a (1/2, -1/2) defect pair. **a)** SEM image of a plasmonic mask with a cluster of 2 topological defects. For imaging clarity, the defect spacing is reduced in comparison to the real mask in **b)**. **b)** Transmission optical image of the plasmonic mask under illumination of non-polarized white light. **c)** Measured polarization field for the plasmonic mask where the background color represents polarization contrast as indicated by the colored scale bar. **d)** Cross-polarized optical microscope of the 2 defects patterned with the mask. **e,** PolScope measured molecular director field. The scale bars in **a-e)** are 1 μm, 2 μm, 2.5 μm, 20 μm and 5 μm respectively. The LC cell gap is about 2 μm.
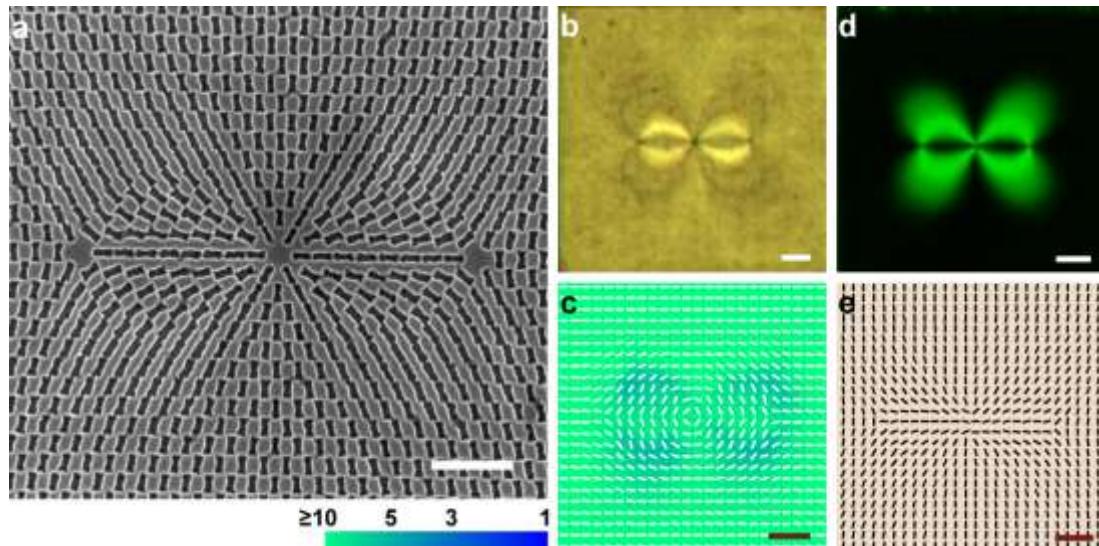
Figure S6. Plasmonic photopatterning of a three defect butterfly. a) SEM image of a plasmonic mask with a cluster of 3 topological defects. For imaging clarity, the defect spacing is reduced in comparison to the real mask shown in b). b) Transmission optical image of the plasmonic mask under illumination of non-polarized white light. c) Measured polarization field for the plasmonic mask where the background color represents polarization contrast as indicated by the colored scale bar. d) Cross-polarized optical microscope of the 3 defects patterned with the mask. e, PolScope measured molecular director field. The scale bars in a-e) are 1 μm, 5 μm, 5 μm, 15 μm and 10 μm respectively. The LC cell gap is about 2 μm.
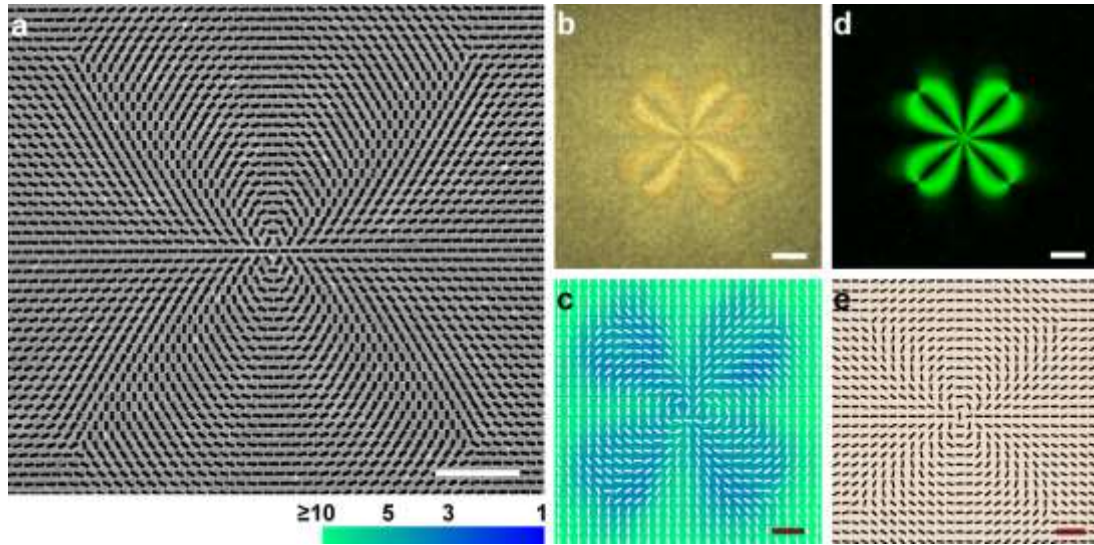
Figure S7. Plasmonic photopatterning of a 5 defect flower. a) SEM image of an illustrative plasmonic mask with a cluster of 5 topological defects. For imaging clarity, the defect spacing is reduced in comparison to the real mask in b). b) Transmission optical image of the plasmonic mask under illumination of non-polarized white light. c, Measured polarization field for the plasmonic mask where the background color represents polarization contrast as indicated by the colored scale bar. d) Cross-polarized optical microscope of the 5 defects patterned with the mask. e) PolScope map of the local optical axis of the LC cell (director field). The scale bars in a-e are 2 μm, 10 μm, 5 μm, 25 μm and 10 μm respectively. The LC cell gap is about 2 μm.
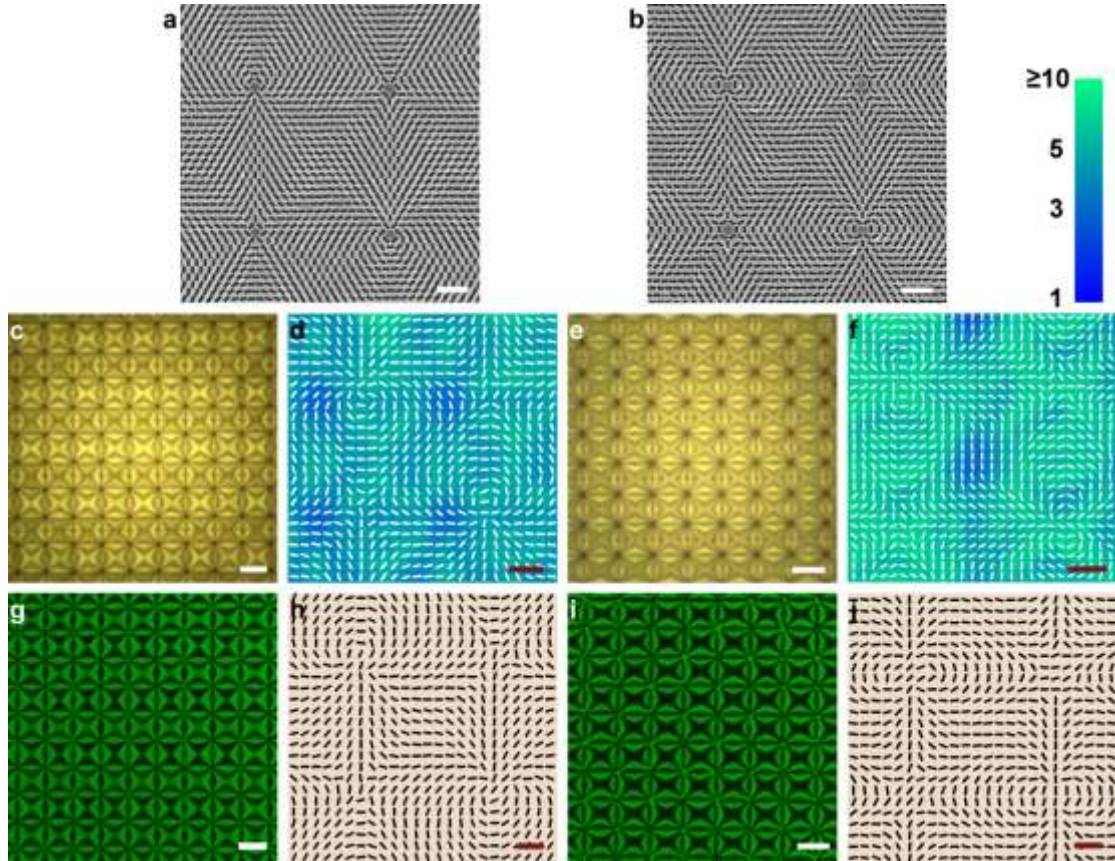
Figure S8. Plasmonic patterning of defect arrays. a,b) SEM images of illustrative plasmonic masks for (+3/2, -3/2) and (+2, -2) topological defect arrays. The defect spacing is reduced from the real masks (shown in c-e) for imaging purpose. c, e) Transmission optical images of the plasmonic masks under illumination of non-polarized white light. d, f) Measured polarization fields for the plasmonic mask c) and e) where the background color represents polarization contrast as indicated by the colored scale bar. g,i) Cross-polarized optical microscopic images of liquid crystal textures patterned with the masks in c) and e). h, j) The LC director fields in g) and i) measured by a PolScope. The scale bars are 1 μm in a) and b), 2.5 μm in d), f), h) and j), 5 μm in c), 10 μm in e), g), and 25 μm in i). The LC cell gap is about 2 μm.

References:

1   O. Yaroshchuk *et al.* in *IDW'07 - Proceedings of the 14th International Display Workshops,* P1665-1668 (2007).
2   Ware, T. H., McConney, M. E., Wie, J. J., Tondiglia, V. P. & White, T. J. Voxelated liquid crystal elastomers. *Science* **347**, 982-984 (2015).
3   Ebbesen, T. W., Lezec, H. J., Ghaemi, H. F., Thio, T. & Wolff, P. A. Extraordinary optical transmission through sub-wavelength hole arrays. *Nature* **391**, 667 (1998).
4   Genet, C. & Ebbesen, T. W. Light in tiny holes. *Nature* **445**, 39-46 (2007).
5   Martin-Moreno, L. *et al.* Theory of extraordinary optical transmission through subwavelength hole arrays. *Phys. Rev. Lett.* **86**, 1114-1117 (2001).
6   Barnes, W. L., Murray, W. A., Dintinger, J., Devaux, E. & Ebbesen, T. W. Surface plasmon polaritons and their role in the enhanced transmission of light through periodic arrays of subwavelength holes in a metal film. *Phys. Rev. Lett.* **92**, 126107 (2004).
7   Liu, H. & Lalanne, P. Microscopic theory of the extraordinary optical transmission. *Nature* **452**, 728-731 (2008).
8   van Beijnum, F. *et al.* Quasi-cylindrical wave contribution in experiments on extraordinary optical transmission. *Nature* **492**, 411-414 (2012).
9   Garcia-Vidal, F. J., Martin-Moreno, L., Ebbesen, T. W. & Kuipers, L. Light passing through subwavelength apertures. *Rev. Mod. Phys.* **82**, 729-787 (2010).
10   Koerkamp, K. J. K., Enoch, S., Segerink, F. B., van Hulst, N. F. & Kuipers, L. Strong influence of hole shape on extraordinary transmission through periodic arrays of subwavelength holes. *Phys. Rev. Lett.* **92**, 183901 (2004).
11   van der Molen, K. L. *et al.* Role of shape and localized resonances in extraordinary transmission through periodic arrays of subwavelength holes: Experiment and theory. *Phys. Revi. B* **72**, 045421 (2005).
12   Ruan, Z. & Qiu, M. Enhanced transmission through periodic arrays of subwavelength holes: The role of localized waveguide resonances. *Phys. Rev. Lett.* **96**, 233901 (2006).
13   Mary, A., Rodrigo, S. G., Martín-Moreno, L. & García-Vidal, F. J. Theory of light transmission through an array of rectangular holes. *Phys. Rev. B* **76**, 195414 (2007).
14   Almeida, E. & Prior, Y. Rational design of metallic nanocavities for resonantly enhanced four-wave mixing. *Sci Rep* **5**, 10033 (2015).
15   Kong, F., Wu, B.-I., Chen, H. & Kong, J. A. Surface plasmon mode analysis of nanoscale metallic rectangular waveguide. *Opt. Exp.* **15**, 12331-12337 (2007).
16   Gordon, R. & Brolo, A. Increased cut-off wavelength for a subwavelength hole in a real metal. *Opt. Exp.* **13**, 1933-1938 (2005).
17   Minh, T. T., Tanaka, K. & Tanaka, M. Complex propagation constants of surface plasmon polariton rectangular waveguide by method of lines. *Opt. Exp.* **16**, 9378-9390 (2008).
18   Dionne, J. A., Sweatlock, L. A., Atwater, H. A. & Polman, A. Plasmon slot waveguides: Towards chip-scale propagation with subwavelength-scale localization. *Phys. Rev. B* **73**, 035407 (2006).
19   Liu, H. & Lalanne, P. Comprehensive microscopic model of the extraordinary optical transmission. *J. Opt. Soc. Am. A* **27**, 2542-2550 (2010).